Giant tunability of Rashba splitting at cation-exchanged polar oxide interfaces by selective orbital hybridization

Giant tunability of Rashba splitting at cation-exchanged polar oxide interfaces by selective orbital hybrization

Hao Xu, Hang Li, Nicolas Gauquelin, Xuejiao Chen, Wen-Feng Wu, Yuchen Zhao, Liang Si, Di Tian, Lei Li, Yulin Gan, Shaojin Qi, Minghang Li, Fengxia Hu, Jirong Sun, Daen Jannis, Pu Yu, Gang Chen, Zhicheng Zhong, Milan Radovic, Johan Verbeeck, Yunzhong Chen,[*] Baogen She

The two-dimensional electron gas (2DEG) at oxide interfaces exhibits extraordinary properties such as 2D superconductivity and ferromagnetism coupled to strongly-correlated electrons in narrow *d*-bands. In particular, 2DEGs in KTaO$_3$ (KTO) with 5*d* t_{2g} orbitals exhibit larger atomic spin-orbit coupling and crystal-facet-dependent superconductivity absent for 3*d* 2DEGs in SrTiO$_3$ (STO). Herein, by tracing the interfacial chemistry, weak anti-localization magneto-transport behavior and electronic structures of (001), (110), and (111) KTO 2DEGs, we discovered unambiguously cation exchange across KTO interfaces. Therefore, the origin of the 2DEGs at KTO based interfaces dramatically different from the electronic reconstruction observed at STO interfaces. More importantly, as the interface polarization grows with the higher order planes in KTO case, the Rashba spin splitting becomes maximal for the superconducting (111) interfaces approximately twice that of the (001) interface. The larger Rashba spin splitting couples strongly to the asymmetric chiral texture of the orbital angular moment, and results mainly from the enhanced inter-orbital hopping of the t_{2g} bands and more localized wave functions. Our finding has profound implications for the search for topological superconductors as well as the realization of efficient spin-charge interconversion for low-power spin-orbitronics based on (110) and (111) KTO interfaces.

1.Introduction

Perovskite oxides are characterized by the presence of narrow-band electrons with *d* orbitals of strongly anisotropic nature and high-Z elements with large spin-orbit interaction. Creating two-dimensional electron gases (2DEGs) at the surface or interface of perovskite oxides, in analogy to those of traditional semiconductors, holds the potential for electronic and photonic functionalities well beyond what we have experienced before.[1–3] Particularly, the Rashba spin-orbit coupling (SOC) effect, where spin degeneracy associated with the spatial inversion symmetry is lifted due to a symmetry-breaking electric field normal to the surface or interface, has led to the discovery of interfacial properties tunability using external electric fields,[4–6]

H. Xu, Y. C. Zhao, Y. L. Gan, S.J. Qi, M. H. Li, F. X. Hu, J. R. Sun, Y. Z. Chen, B. G. Shen
Beijing National Laboratory of Condensed Matter Physics and Institute of Physics
Chinese Academy of Sciences
Beijing 100190, China
Email: yzchen@iphy.ac.cn;
H. Xu, Y. C. Zhao, Y. L. Gan, S.J. Qi, M. H. Li, F. X. Hu, J. R. Sun, Y. Z. Chen, B. G. Shen
School of Physical Sciences, University of Chinese Academy of Sciences, Beijing 100049, China;
H. Li, M. Radovic
Photon Science Division, Paul Scherrer Institute, 5232 Villigen-PSI, Switzerland
N. Gauquelin, D. Jannis, J. Verbeeck
Electron Microscopy for Materials Science (EMAT), University of Antwerp, 4Groenenborgerlaan 171, 2020 Antwerp, Belgium
X. J. Chen, Z. C. Zhong, B. G. Shen
CAS Key Laboratory of Magnetic Materials and Devices and Zhejiang Province Key Laboratory of Magnetic Materials and Application Technology, Ningbo Institute of Materials Technology and Engineering, Chinese Academy of Sciences, Ningbo 315201, China

W. F. Wu
Key Laboratory of Materials Physics, Institute of Solid State Physics, HFIPS, Chinese Academy of Sciences, Hefei 230031, People's Republic of China
Science Island Branch of Graduate School, University of Science and Technology of China, Hefei 230026, People's Republic of China
L. Si
School of Physics, Northwest University, Xi'an 710127, China
D. Tian, P. Yu
State Key Laboratory of Low Dimensional Quantum Physics and Department of Physics, Tsinghua University, Beijing, 100084 China
L. Li
Frontiers Science Center for Flexible Electronics, Xi'an Institute of Flexible Electronics (IFE) and Xi'an Institute of Biomedical Materials and Engineering, Northwestern Polytechnical University, 127 West Youyi Road, Xi'an 710072, China
G. Chen
Department of Physics and HKU-UCAS Joint Institute for Theoretical and Computational Physics at Hong Kong, The University of Hong Kong, Hong Kong, China
B. G. Shen
Ganjiang Innovation Academy, Chinese Academy of Sciences, Ganzhou, Jiangxi 341000, China
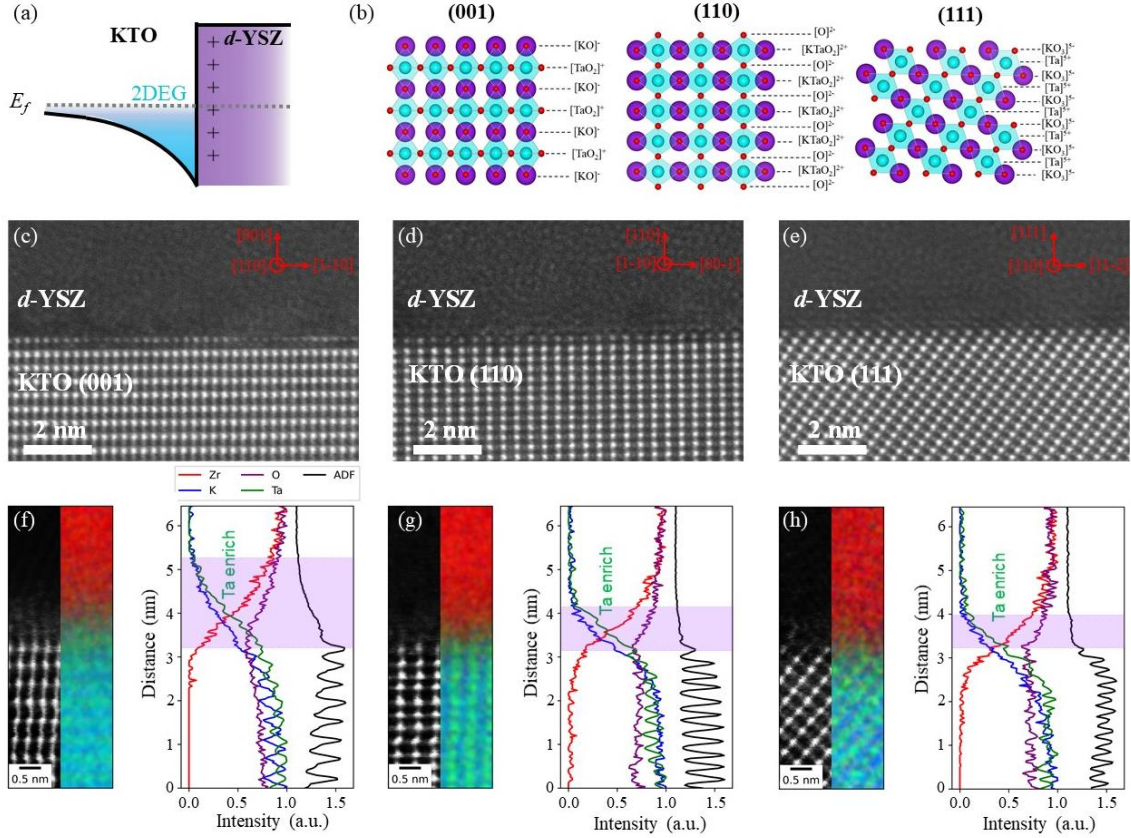
Fig.1 (a) Schematic of the *d*-YSZ/KTO interfacial 2DEGs; (b) Sketch of the polarity for the KTO crystals of (001), (110) and (111) faces; (c)-(e) STEM images of the (001), (110) and (111)-oriented *d*-YSZ/KTO samples, respectively, viewed along the <110> orientation. (f)-(h) EELS experimental maps across the *d*-YSZ/KTO interfaces showing the Ta M (green), Zr L (red), and K L (blue) edges, respectively, for the (100), (110) and (111) orientations. Each interface shows a higher Ta\K ratio in the interfacial region as well as a lower oxygen content than in the rest of the YSZ film and the KTO substrate.

as well as gate voltage control of the spin precession for spin-orbitronic devices.[7] The nontrivial Rashba spin splitting can lead to efficient spin-charge interconversion at oxide interfaces,[8,9] where the spin current generation, spin detection, and the manipulation of the magnetization can be tuned by electric fields, offering one of the most promising routes towards low-power spintronics.[10] Moreover, a sizable SOC could drive the formation of a host of unconventional Cooper pairing and for the realization of Majorana states.[11]

The prototypical oxide 2DEG is formed when $SrTiO_3$ (STO) is interfaced with a polar perovskite of $LaAlO_3$ (LAO).[12–16] Such 3*d* 2DEG originates from the polarity-discontinuity-induced electronic reconstruction,[12,17] which exhibits extraordinary properties, such as 2D superconductivity,[13] magnetism,[14,15] and multi-well quantum Hall effect.[16] Similar 2DEGs can also be formed by interfacial redox-reactions[18,19] or exposure of STO single crystals to Ar$^+$ ions and even under intense ultraviolet light illumination in high vacuum.[20,21] The

carriers of these STO 2DEGs are derived from the Ti t_{2g} orbitals, and the strength of their Rashba SOC exhibits a dome feature as a function of the band filling with a maximal spin splitting energy Δ~3-6 meV near the crossing point of the d_{xy} and d_{xz}/d_{yz} orbitals, as inferred from the presence of weak anti-localization (WAL) in magneto-transport experiments.[4,6,22–25] So far, the tunability of the Rashba splitting has relied largely on the control of carrier density by electrostatic gating or light-illumination. Despite intensive research, a crucial question that remains elusive is how to maximize the magnitude of the Rashba parameters for as-grown oxide 2DEGs without the application of external fields.[2,25]

It is generally accepted that materials possessing heavy elements display larger spin splitting due to their large atomic SOC. In this vein, the 5*d* 2DEG at the surface/interface of $KTaO_3$ (KTO),[9,21,26–31] another cubic quantum paraelectric perovskite insulator presenting a stronger atomic SOC (~ 0.47 eV) more than one order of magnitude larger than that of STO (~ 0.02

1

eV), has attracted great interest recently.[9] Analogous to the case of STO 2DEGs, the vast majority of studies on KTO 2DEGs have been focused on the (001)-oriented faces.[9,21,26,27] The evolution of the shape of the Fermi surface, the effective masses of the states and the orbital ordering for these (001) interfaces have been found to exhibit similar trends to those of 3d STO 2DEGs as varying the charge carrier density.[31,32] However, the roles of crystalline symmetry, the interfacial polarity as well as the non-centrosymmetric electrostatic potential that surrounds these atoms on the Rashba spin splitting remain open. Notably, STO 2DEGs are superconducting at around 300 mK with no significant dependence on the orientation of the crystal plane.[13,33] However, a clear orientation-dependent superconductivity phenomenon was recently discovered at KTO interfaces,[28–31] i.e. while the KTO 2DEGs show no interfacial superconductivity down to 50 mK along (001) direction but higher transition temperatures up to 0.9 K and 2.2 K were detected for (110) and (111) oriented samples, respectively.[28–30] These features call for studying in detail the crucial importance of the crystalline orientation on the pairing mechanism, electron-phonon coupling

as well as the orientation-dependent Rashba SOC in KTO surfaces/interfaces.

Herein, by combining aberration-corrected scanning transmission electron microscope (STEM), WAL magneto-transport measurement, Circular Dichroism angle resolved photoemission spectroscopy (CD-ARPES), and density functional theory (DFT)-based tight-binding calculations for KTO 2DEGs in (001), (110) and (111) orientations, we find that the Rashba SOC of KTO interfaces exhibits a surprising sensitivity to the crystal facet-orientation thus the inter-orbital hopping. The magnitude of the spin splitting, is the highest for the superconducting (111) faces, which is slightly higher than that of (110) faces, and more than two times higher than that of (001) faces. CD-ARPES experiments and DFT calculations reveal that the crystal-facet-dependent Rashba SOC is coupled strongly to the change in the orbital angular moment, where the spin splitting is determined mainly by the inter-orbital hopping of the t_{2g} bands. The results reveal the significant potential of KTO 2DEGs of (110) and (111) orientations for efficient spin-charge interconversion as well as the design of topological superconductors.

2. Results and discussion

2.1 Creation of 5d 2DEGs at KTO (001), (110), and (111) interfaces with unforeseen cation-exchange reconstructions

Our KTO 2DEGs (Fig.1a) were fabricated at room temperature by depositing disordered yttria-stabilized zirconia (d-YSZ) thin films on top of the single crystalline KTO substrates with (001), (110), and (111) orientations, which not only exhibit strong interfacial redox reactions but also excellent stability in ambient environment [19]. The room temperature deposition could rule out any cation-intermixing induced by high-temperature procedures such as annealing. As shown in Fig. 1b, the formal charges for K, Ta, and O ions are +1, +5, and -2, respectively, thus in the ideal ionic limit, the (001) KTO surface consists of alternative [TaO$_2$]$^+$ and [KO]$^-$ planes with formal positive and negative charges, whereas the (110)- and (111)-oriented KTO surfaces exhibit stronger polar discontinuity with the alternate stacking sublayers of [KTaO]$^{4+}$/[O$_2$]$^{4-}$ and [Ta]$^{5+}$/[KO$_3$]$^{5-}$, respectively. Therefore, all d-YSZ/KTO interfaces are highly polar. As the crystalline orientation varies from (001) to (110) and (111), the polar discontinuity, thus the divergence of electrostatic energy, increases. In general, the field generated by the dipole plane will lead to re-

arrangements/screening by electronic charge transfer, atomic reconstructions, or chemical doping, accompanied with the possible emergence of unusual electrical and physical properties.[34] For the intensively-investigated polar LAO/STO interfaces, the interface polarity is compensated largely by pure electronic reconstructions in proximity to the mixed-valence Ti states[17]. Besides the formation of the 2DEG, ferroelectric displacements instead of cation intermixing often occur that create local dipole moments opposed to the internal electric field in order to compensate the polar catastrophe.[35]

As shown in Figs. 1c-e, the three d-YSZ/KTO samples with different orientations all show clearly-defined amorphous-YSZ/crystalline KTO interfaces as determined by cross-sectional STEM along the <110> orientation in the high-angle annular dark field (HAADF) imaging mode, where the KTO part is unexpectedly terminated with Ta-containing sublayers, although the substrates were started from the coexistence of both KO and TaO$_2$ terminations. Further in depth analysis of the chemical composition across the interfaces with atomically resolved electron energy loss spectroscopy (EELS) identifies a cation-exchanged interfacial region with the depletion of K and enrichment of Ta of approximately 2.0 nm, 1.0 nm, and 0.8 nm, respectively, where one boundary is defined as the last

crystalline atomic plane of the KTO substrate and the other is the distance for which the Ta has dropped below 5% of its bulk normalized EELS intensity, for the (001), (110) and (111) interfaces (Figs. 1f-h). Notably, there are no detectable lattice distortions for the K and Ta cations of the KTO hetero-interfaces, although displacements of Ta and O atoms perpendicular to the surface are probable due to the deficiency of the oxygen near the interface. These results strongly suggest that, in contrast to the electronic interface reconstruction of LAO/STO, the KTO interfaces exhibit unusual cation-exchange reconstructions as consequences of compensating the interface dipole energy.[36] Although the formation of striped structure consisting of equally exposed KO and TaO_2 stripes was recently revealed by atomic force microscopy (AFM) and scanning tunneling microscopy (STM) measurements in vacuum on (001) oriented KTO surfaces,[37] the observation of cation-exchanged reconstruction at conducting oxide interfaces has not been reported experimentally so far, to the best of our knowledge. It probably originates from the K ions migrating upwards from the subsurface into the capping layer driven by the highly charged small Ta cation eager to gain a higher coordination.[36] It remains open whether or not the oxygen vacancies contribute to the cation intermixing. But we observe clear oxygen deficiency at the interfacial region for the three differently oriented interfaces, and since the interface conduction, originating from the states on the Ta ions, could be annihilated upon oxygen annealing at 200 °C, interfacial redox reaction should also contribute to this interfacial conduction.[30] Based on these results, we can propose that cation exchange reconstruction in combination with redox-reaction induced oxygen vacancies are crucial for the formation of KTO 2DEGs.

2.2 Crystal-facet-dependent Rashba SOC of KTO 2DEGs determined by WAL magnetoresistance

Fig. 2a shows the temperature-dependent sheet resistance for d-YSZ/KTO heterointerfaces with (001), (011), and (111) orientations, measured along [100], [1-10] and [11-2] in-plane directions, respectively. All samples present metallic behavior for temperatures from 2-300 K. By further cooling to the diluted temperature of 50 mK, superconductivity is observed in the (111) interface with the superconducting transition

temperature T_c=0.61 K, which is close to the lower limit of those (111) KTO heterointerfaces grown at high temperatures according to the linear dependence of T_c on sheet carrier density n_s,[38] and approximately twice the maximal T_c of LAO/STO.[13,33] The n_s of these samples is determined by Hall measurement, which is linear at room temperature for all samples with electrons as the dominant carrier. The linear Hall effect persists down to 2 K for (110)- and (111)- interfaces with a carrier density of approximately $n_{110} \sim 6.9 \times 10^{13}$ cm^{-2} and $n_{111} \sim 7.3 \times 10^{13}$ cm^{-2}, respectively. Both are above the typical Lifshitz transition point, $n_c \approx 4.1 \times 10^{13}$ cm^{-2} for KTO 2DEGs.[31,32] However, the (001)-interface exhibits a nonlinear Hall effect at $T<$ 20 K due to the presence of two-band conduction (Supplementary Fig. S3). The analysis of the nonlinear Hall resistance with the two-conduction channel model gives rise to a total $n_{001} \sim 6.7 \times 10^{13}$ at 2 K. Shortly, our KTO 2DEGs of different orientations share similar total sheet carrier density n_s in the order of $\sim 6.5\text{-}7.5 \times 10^{13}$ cm^{-2} or the Fermi energy ($E_F = n_s \pi \hbar^2/m$ with $m = 0.36m_e$) of ~ 500 meV thus comparable quantum confinement and a mobility of $\mu \sim 150$ cm^2/Vs at 2 K (Supplementary Fig. S4). Experimentally, the strength of the Rashba SOC can be deduced from WAL analysis from the magnetoresistance ($MR, [R(B) - R(0)]/R(0)$) results.[4,16,19–22,33–35] Figs. 2e-g present the MR versus B curves for the three crystal orientations at low temperatures. For (001) interfaces, the observed MR is typically positive and increases quadratically in high fields, which implies an ordinary MR described by the Kohler's rule. However, for (110) and (111) interfaces, particularly at $T<$10 K, the field dependent MR curves exhibit a clear cusp around B=0, which is the typical feature of WAL in weak localization (WL) systems. Followed by the WAL induced cusp, the presence of parabolic magnetoresistance at high magnetic fields implies the contribution from the ordinary MR as observed for (001) interfaces. Upon increasing temperature, the cusp around B=0 becomes broad and gradually disappears due to decreasing WL. The WAL originates from the destructive interference of electron waves propagating in time-reversal closed trajectories induced by Rashba SOC, where the SOC suppresses quantum backscattering induced WL.[4] Therefore, it turns out that the (111) interface exhibits the most robust WAL behavior thus the Rashba SOC effect.
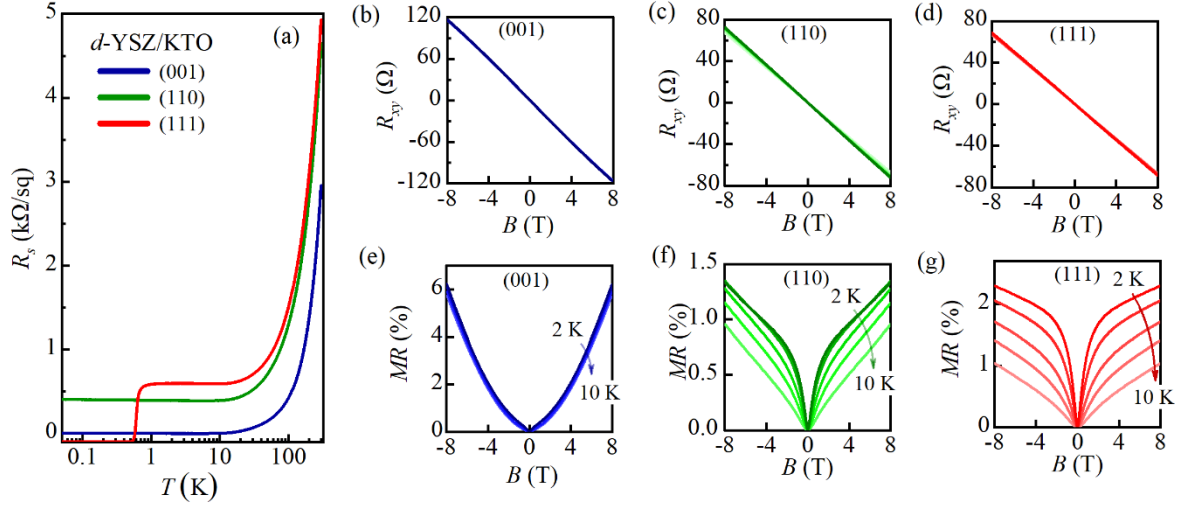
FIG.2 (a) Temperature dependence of the sheet resistance for (001), (110) and (111) d-YSZ/KTO interfaces measured in the temperature range of 50 mK-300 K measured along [100], [1-10] and [11-2] in-plane directions, respectively; (b)-(d)Hall resistance R_{xy} with respect to magnetic field for (001), (110) and (111) oriented d-YSZ/KTO 2DEGs, respectively, at 2 K-10 K; (e)-(g) The magnetic-field-dependent magnetoresistance for (001), (110) and (111) oriented d-YSZ/KTO 2DEGs, respectively, at 2 K-10 K. Magnetic field B is applied out-of-plane in the normal states.
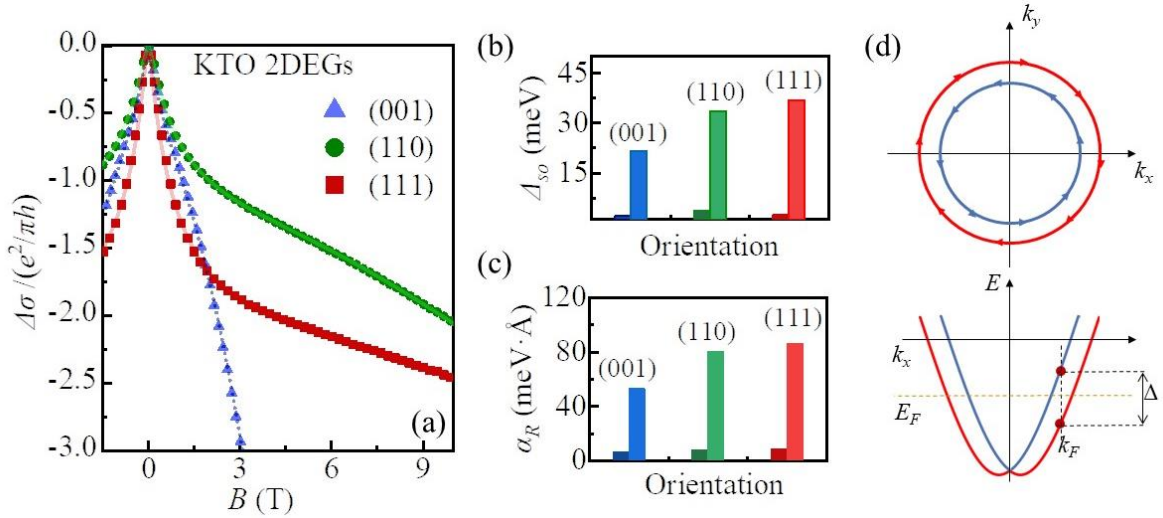

FIG.3 (a) The fits of normalized magnetoconductance to the Maekawa-Fukuyama theory for (001), (110) and (111) oriented d-YSZ/KTO interfaces at 2 K. (b) and (c) illustrate, respectively, the spin splitting energy Δ_{so}, and the Rashba coefficient α_R as a function of the crystal-facet-orientations of KTO 2DEGs (right). For comparison, the typical values for STO 2DEGs are also shown (left). (d) The qualitative sketch of the Fermi surface/interface in xy plane and the Rashba effect.

Experimentally, the strength of the Rashba SOC can be deduced from WAL analysis from the magnetoresistance (MR, $[R(B) - R(0)]/R(0)$) results.[4,16,19–22,33–35] Figs. 2e-g present the MR versus B curves for the three crystal orientations at low temperatures. For (001) interfaces, the observed MR is typically positive and increases quadratically in high fields, which implies an ordinary MR described by the Kohler's rule.

However, for (110) and (111) interfaces, particularly at T<10 K, the field dependent MR curves exhibit a clear cusp around B=0, which is the typical feature of WAL in weak localization (WL) systems. Followed by the WAL induced cusp, the presence of parabolic magnetoresistance at high magnetic fields implies the contribution from the ordinary MR as observed for (001) interfaces. Upon increasing temperature, the cusp around B=0

becomes broad and gradually disappears due to decreasing WL. The WAL originates from the destructive interference of electron waves propagating in time-reversal closed trajectories induced by Rashba SOC, where the SOC suppresses quantum backscattering induced WL.[4] Therefore, it turns out that the (111) interface exhibits the most robust WAL behavior thus the Rashba SOC effect.

To quantify the Rashba SOC strength, the 2D localization theory in diffusion regime developed by Maekawa–Fukuyama (MF) with the D'yakonov–Perel mechanism of spin relaxation is employed to analyze the WAL induced quantum correction on magneto-conductance.[4] The total magneto-conductance can be expressed as:

$$\frac{\Delta\sigma_{xx}(B)}{G_0} = -\psi\left(\frac{1}{2} + \frac{B_e + B_{so}}{B}\right) + \psi\left(\frac{1}{2} + \frac{B_i + B_{so}}{B}\right)$$
$$+ \frac{1}{2}\psi\left(\frac{1}{2} + \frac{B_i + 2B_{so}}{B}\right) - \frac{1}{2}\psi\left(\frac{1}{2} + \frac{B_i}{B}\right)$$
$$- \left[ln\left(\frac{B_i + B_{so}}{B_e + B_{so}}\right) + \frac{1}{2}ln\left(\frac{B_i + 2B_{so}}{B_i}\right)\right]$$
$$- A_k \frac{\sigma_{xx}(0)}{G_0} \frac{B^2}{1 + CB^2}$$

Here, $\psi(x)$ is the digamma function and $G_0 = e^2/\pi h$. The three characteristic magnetic fields $[B_k = \hbar/(4eD\tau_k), k = i, e, so]$ characterize the B-dependent quantum correction contributed from three scattering processes with τ_i, τ_e, and τ_{so} being the inelastic scattering time, the elastic scattering time, and the spin-orbit scattering time, respectively. The last term from Kohler's rule describes the ordinary magneto-conductance with fitting parameters A_k and C. The best fits at 2 K (Fig. 3a) give rise to B_{so} of 0.41 T, 0.95 T and 1.1 T for (001), (110) and (111) interfaces respectively, and the corresponding spin splitting energy $\Delta_{so} = 2\alpha_R k_F$ ($\alpha_R = \frac{\sqrt{e\hbar^3 B_{so}}}{m}$ is Rashba coefficient and $k_F = \sqrt{2\pi n_s}$ is the Fermi wave vector and the average effective mass $m = 0.36m_e$) is summarized in Fig. 3b. Overall, the Rashba SOC of KTO 2DEGs show two significant features in comparison to STO 2DEGs. First of all, the Rashba spin splitting of the $5d$ 2DEG is approximately 10 times larger than that of STO 2DEGs (Δ_{so}= 2-4 meV) along all the three facets with α_R up to ~ 80 $meV\text{Å}$ (Fig. 3c). Secondly, the Rashba spin splitting shows strong orientation dependence, where the highest Δ_{so} of 36.94 meV is observed for the highly symmetric (111) interface, which is slightly higher than that of (110) faces and approximately twice as that of the (001) interface (Δ_{so}=21.75 meV

at 2 K). It is noteworthy that such facet-dependent Rashba spin splitting has not been observed previously for STO 2DEGs.[6,24]

2.3 ARPES and circular-dichroic ARPES of KTO Surface 2DEGs with different orientations

Figs. 4a-c present the Fermi surface (FS) topography for KTO surface 2DEGs with (001), (110), and (111) orientations, respectively, where the symmetry of the FS features reflects the in-plane atomic symmetry of each orientation. The Fermi pockets at E_F are marked by white guided dashed lines (Figs. 4a-c) for better illustration. For the (001) orientation, the tetragonal KTO surface preserves the four-fold symmetry, resulting in an FS with two intersecting ellipse electron pockets and one circular electron pocket centered at the Γ point (Fig.4a), belonging to the d_{xz}/d_{yz} and d_{xy} orbitals, respectively.[21] In contrast to the tetragonal (001) orientation, only orthorhombic symmetry is preserved for the (110) face, resulting in a two-fold FS structure (Fig. 4b). The ellipse electron pocket with the long axis along the Γ-Z direction belongs to the d_{xy} orbitals, while the d_{xz}/d_{yz} orbitals contribute to the other ellipse pockets with the long axis along Γ-M direction.[39] Unlike the inequivalent t_{2g} bands in the (001) and (110) orientations, the FS of the (111)-oriented KTO surface consists of three ellipses electron pockets with the long axis along the Γ-M direction, forming a sixfold symmetric Star-of-David like FS structure as observed for (111) STO 2DEGs.[40] These identical FSs correspond to the equivalent t_{2g} bands (one a$_{1g}$ state and two e'$_{2g}$ states[15]) protected by the trigonal symmetry of the (111) face (Fig. 4c). However, due to the limitations in energy and momentum resolution, the Rashba-type SOC splitting (with the typical value of ~30 meV) is hardly identified from the electronic structure, as demonstrated in former studies.[39,41,42]

Nevertheless, the asymmetry in the circular dichroism ARPES (CD-ARPES) signal is another direct evidence of the chiral orbital angular momentum (OAM) structure induced by strong SOC.[43,44] Figs. 4d-f show the behavior of CD-ARPES of our KTO 2DEGs with different orientations, calculated by A(k)=[I$_R$(k) - I$_L$(k)]/[I$_R$(k) + I$_L$(k)], in which I$_{R/L}$(k) represents the photoemission intensities probed by right-/left- circular light, respectively. As the crystal orientation varies from (001), (110) to (111), the CD asymmetry increases strongly. To make this clear, we extracted the CD asymmetry values along the edge of each ellipse pocket (marked by dashed curves in Figs. 4a-f) at the Fermi level (E$_F$), and plotted them as a function of the included angle between k$_F$ and k$_x$, as shown in Figs. 4g-i for

(001), (110), and (111) faces, respectively. The maximal CD asymmetry of (001) KTO 2DEG is only 0.15, while the magnitude increases significantly to ~0.4 for (110)-orientation surface, and up to ~0.6 for KTO (111) faces. For (111) KTO 2DEG, the CD-asymmetry is even larger than the classical Bi_2Se_3.[45] The CD asymmetry associates strongly to spin-texture and OAM related to Rashba spin splitting.[43] For our KTO 2DEGs, the inversion symmetry is broken due to the electric field normal to the surface, while the time-reversal symmetry is preserved. It should be noticed that due to the complexity of 5d system, the robust connection between non-quenched OAM and CD-asymmetry is not established. The orientation-dependent CD-asymmetry still reflect the strength of orientation sensitive OAM and can be considered as signature of the Rashba-split thus further confirms the orientation-dependent Rashba SOC in KTO 2DEGs.

The change in spin-orbit coupling affects not only the ground state properties but also the dynamical properties such as the electron-phonon interaction (EPI), another important ingredient of the electronic properties. The EPI, which is embedded in the spectral function $A(\omega,k)$ represented by the energy distribution curves (EDCs) of the ARPES intensity, can be deduced by analyzing the quasiparticle residue (Z_0) of the peak-dip-hump structure in ARPES spectra.[46] The fitted Z_0 of KTO with different orientation shows a decrease from (001) to (110) and (111) orientation (see in Supplementary Materials Figure S6), indicating the increase of the strength of EPI. The weak EPI in (001) KTO surface/interface may explain the absence of superconductivity, consistent with the fact that when a $LaMnO_3$ bufffer is introduced at the LAO/STO interface,[47] the EPI is reduced and the superconductivity disappears.[48] We noticed that there are also recent studies showing that KTO interfaces with higher T_c exhibit stronger EPI.[38,49]
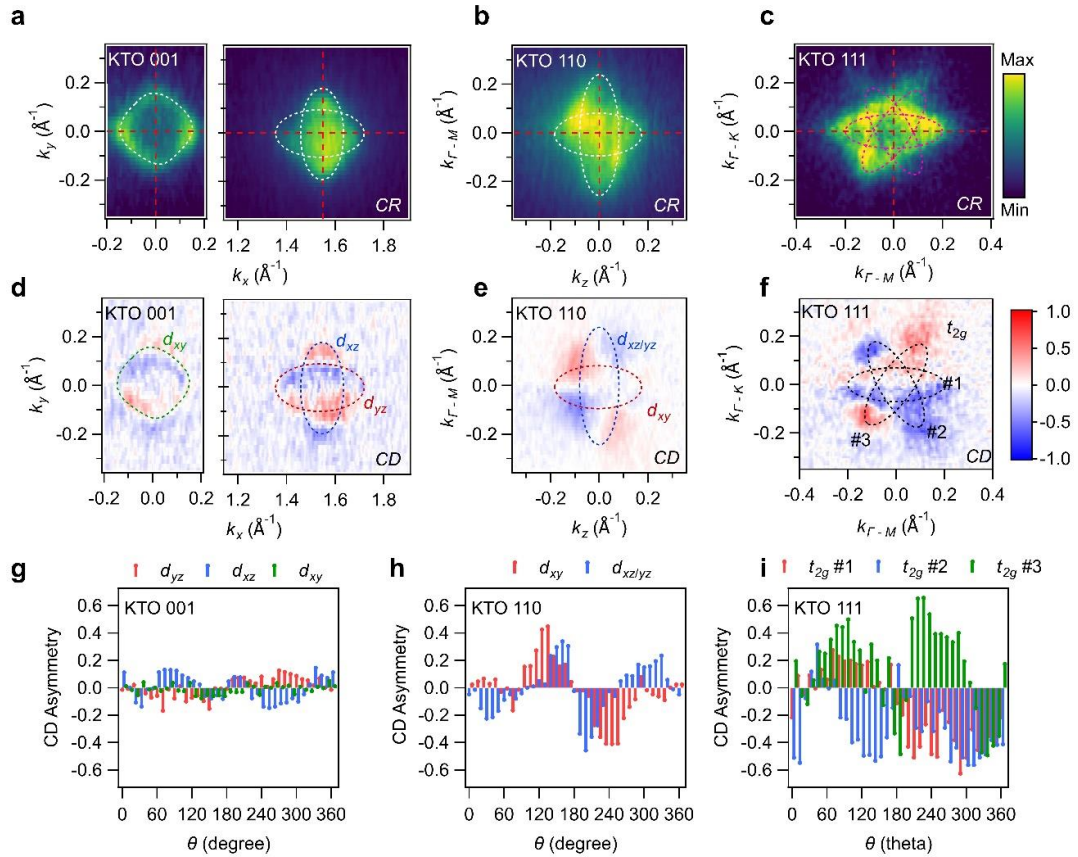

Figure 4. (a)-(c), in-plane ARPES intensity maps of (001), (110), and (111) oriented KTO surfaces, respectively. All maps are measured by circular polarization. (d)-(f), The corresponding circular dichroism asymmetry maps of KTO surfaces with different orientations. Dashed curves in (a)-(f) with different color illustrate the fermi pockets contributed by different orbitals. (g)-(i), CD asymmetry extracted from the k_F of pockets in (d)-(f), respectively, for (001), (110), and (111) oriented KTO surfaces.

2.4 First principles crystal and electronic structure analysis for different orientation of KTO interfaces

To elucidate the heightened Rashba spin-orbit coupling (SOC) and electron-phonon interactions (EPI) observed in (110) and (111) orientation KTO films, we conducted a comprehensive analysis encompassing structural and electronic structure examinations. Additional DFT results, including orbital-projected spectra, surface spectra, can be found in Supporting Information Fig.S7-S15 and Table S1. The adoption of two non-symmetric surface termination configurations, representing the top and bottom slabs in our computational models, yield to an internal inversion symmetry-breaking field. This perturbation eliminates the inversion symmetry between the top and bottom slabs in the models, and influencing the amplitude of Rashba-like effects along (001), (110), and (111) directions.

Commencing our analysis with the fundamental setup of (001) orientation interfaces, we anticipate lattice and orbital polarization due to surface relaxation (also see Fig.S7 and S10). Consequently, non-zero inter-orbital hoppings are observed. For example, along the x direction [R=(100)], a non-zero hopping between d_{xy} and p_y orbitals emerges, a feature absent in bulk KTO due to crystal rotational symmetry. The Rashba spin splitting is then induced by the combination of intrinsic SOC and the breaking of crystal inversion symmetry, as illustrated in Fig. 5a. Expanding our investigation to (110) and (111) slabs using the slab models we observe, in Figs. 5b and c, that in proximity to Γ, the spin splittings in (110) and (111) are 4.2 meV and 1.0 meV, respectively, both more than five times larger than those in the (001) orientation slabs (0.17 meV). As we move away from Γ, the spin splitting intensifies, reaching a maximum of around 28 meV for the (110) surface at 0.6 Å^{-1} along Γ to M. The α_R deduced by fitting the Rashba spin splitting of the DFT-based calculations are 20 meVÅ, 106 meVÅ, and 77 meVÅ for (001), (110), and (111) slabs, respectively. With stronger electronic correlations and enhanced electric polarization induced by $(KO_3)^{5-}$ and Ta^{5+} atomic layers in the (111) surface, we expect the experimentally observed Rashba splitting to be more pronounced compared to that observed in the (110) surface. Please note that the Fermi surfaces observed in our ARPES measurement for (001), (110), and (111) surfaces exhibit signals within 0.2 A^{-1} [Fig.4(a-c)]. These observations

align with the DFT simulations (Fig. S15), indicating Fermi surfaces at 2.5-2.6 eV, 2.5-2.6 eV, and 2.45-2.6 eV for (100), (110), and (111) surfaces, respectively. On the whole, this calculated spin splitting trend aligns with experimental observations of crystal-symmetry-enhanced spin splitting.

3. Discussion and Conclusions

Rashba effects are phenomena caused by spin–orbit interaction and broken mirror symmetry, which is associated with electric field perpendicular to the 2DEG plane. Therefore, Rashba interactions can be tuned not only by tunning spin-orbit interaction but also altering the perpendicular external electric fields and/or oxygen-metal sublattice relative displacements[50]. The strong dependence of the Rashba spin-splitting on crystallographic orientation is reminiscent of the theoretical prediction that the Rashba interactions in complex oxide 2DEGs are due primarily to changes in metal-oxygen-metal bond angles at surfaces and interfaces[50]. It is the interorbital perturbed hopping terms between the energy bands that determines the Rashba-like SOC effect. As far as the (001) face is considered (Fig.5d), the Hamiltonian H_z term generates electronic hopping from d_{xy} to d_{zx} along the y direction via p_x and from d_{xy} to d_{yz} along the x direction via p_y in the second-order perturbation producing the Rashba-like SOC effect, which is forbidden in the distortion-free system. The t_{2g} bands of (001) interfaces often show the d_{xy} band lower than the d_{yz}/d_{zx} bands thus negligible Rashba splitting due to weak overlap integration with O-$2p_z$ orbital and C4v point group giving limited crystal field value, which in final creates small orbital-dependent asymmetry response ability although the splitting becomes largest near the band crossing[5]. As the orientation varies, the degeneracy of three t_{2g} orbitals is split differently in their confinement energies. For the (111) interfaces, the three t_{2g} orbitals are degenerate and equivalent modulo a rotation of 120° when viewed along the surface normal (Fig.5e). Consequently, the number of d orbitals participating in the interorbital hopping are maximal. In the meantime, the electron phonon coupling strength and the interorbital hopping for the KTO (110) surface is intermediate because the inversion symmetry breaking does not occur along the [001] crystal axis in the (110) plane, reflecting the reduced orbital degeneracy of (110) relative to (111). Similar conclusion can also be deduced based on the orbital projected band structures obtained from first principles tight-binding calculations on ideal (001), (110) and (111) KTO slab structures using bulk Ta 5d and O 2p orbital projected Wannier localized

states as illustrated in Fig. 5a–c. Additionally, the Rashba spin-splitting is also strongly related to the localization of the wave function at the interface[51]. To further check the effect of localization of the wave function at the interface on the facet dependent Rashba spin splitting, we computed the density of states of (001), (110) and (111) KTO monolayer sandwiched by several layers of STO, which give raise to the narrowest bandwidths of Ta-5d t_{2g} bands and smallest Wannier spreads for the (111) facet KTO 2DEGs (Fig.S16 and Table S2). Given the more localized wave functions and the reduction in the electron-hopping term along the in-plane direction of (110) and (111) orientations, the off-diagonal elements arising from Rashba interaction lead to larger Rashba splitting and α_R.

In short, the KTO surface/interfaces show a high sensitivity of interfacial superconductivity as well as strong dependence of

Rashba SOC to crystallographic orientation. The (111) interfaces turn out to show the highest T_c, strongest EPI and the largest Rashba SOC. Based on the predictions for the existence of novel topological and multi-ferroic phases in (111) bilayers of ABO_3 cubic perovskites[52], the B site ions (Ta) of a bilayer resemble a honeycomb lattice (Fig.5e), similar to that of graphene and topological insulators such as Bi_2Se_3. The presence of strong spin-orbit coupling and broken inversion symmetry at (111) KTO interfaces could enable new channels for Cooper pairing, and for realizing Majorana states. The large Rashba SOC strength also implies efficient spin-charge interconversion. Therefore, our findings highlight the untapped potential of (110) and (111) KTO 2DEGs as a playground for unconventional quantum states and spintronic applications.
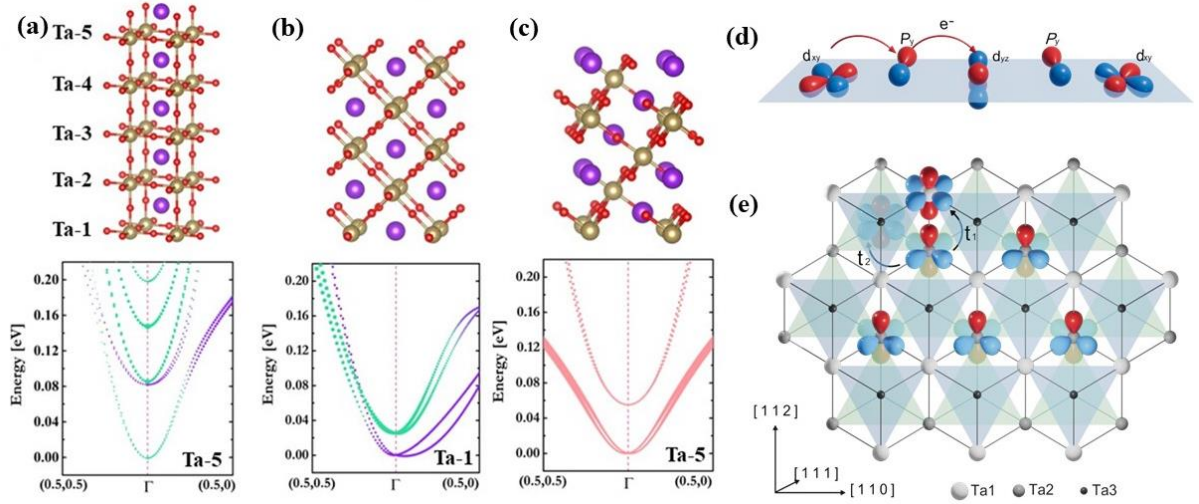

Fig. 5 (a)-(c) Slab structures and orbital projected layered-dependent band structures for (001), (110), and (111) KTO surfaces, respectively, based on first principles tight-binding calculations. The band characters from d_{xy} and d_{yz}/d_{xz} orbitals are represented by green and purple colors in (a) and (c), respectively. In the case of the (111) surface, the bands are depicted in red, as the d_{xy}, d_{yz}, and d_{xz} orbitals in this configuration exhibit strong hybridization/mixing due to the symmetry. (d) Schematic of the Rashba effect due to the interorbital hopping of (001) interfaces with lattice polarization; (e) Top view of three consecutive Ta-based (111) layers. Each of the three t_{2g} orbitals are shown on the honeycomb lattice, formed by two consecutive layers (dark grey lines), to illustrate their rotational symmetry. The large (t_1) and small (t_2) nearest neighbor hoppings are also indicated.

4. Methods

4.1 Sample preparation and transport measurements

All heterostructures were grown on $KTaO_3$ (KTO) single crystal substrates ($5\times5\times0.5$ mm^3) with (001), (110), and (111) orientations by pulsed laser deposition (PLD) from a single-crystalline YSZ target in an oxygen atmosphere of 1×10^{-6} mbar at room temperature. During ablation, a KrF laser (λ=248 nm)

with a repetition rate of 1 Hz and laser fluence of 1.5 J cm^{-2} was used. The target-substrate distance was fixed at 5.5 cm.

Electrical characterization was performed on a Physical properties measurement system (PPMS) with the temperature down to 2 K and magnetic field up to 16 T. The samples were patterned into Hall-bar configuration with ultrasonically wire-bonded aluminum wires as electrodes.

4.2 STEM and EELS analysis.

Transmission electron microscopy imaging studies were performed at room temperature using the Qu_Ant_EM microscope, which is an aberration-corrected scanning transmission electron microscope (STEM), Thermofisher Titan3 80-300 operated at an acceleration voltage of 300 kV, equipped with a high-brightness field-emission electron source (X-FEG). Cross-sectional cuts of the samples grown under the optimum condition described above were prepared using a dual-beam focused ion beam (FIB) instrument. For HAADF imaging, a probe size of approximately 1Å with a convergence angle of 20 mrad, and an HAADF collection semi-angle of 70-160 mrad were used.

For electron energy-loss spectroscopy (EELS) in STEM, a Thermofisher Titan ThemisZ was used, the collection semi-angle was set to 40 mrad. Spectrum images (SI) were acquired at 200kV and a beam current of 30pA to reduce beam damage and an acquisition time of 12ms/pixel and a pixel size of 0.3A. Low and core loss were acquired almost instantaneously with a dispersion of 0.7eV/pixel. Model based fitting procedure[53] was used to extract the elemental maps where a linear background model was used.[54] In order to improve the signal-to-noise, the edge shapes of the different elements were extracted from the average EEL spectrum by doing an interpolation of the near edge structure[55] together with the atomic cross section.[56] These new edge shapes were used as input model for the fitting of the spectrum image.

4.3 Angle-Resolved Photoemission Spectroscopy (ARPES).

The vacuum ultra violet ARPES measurements were performed at the SIS-Ultra beamline of the Swiss Light Source at Paul Scherrer Institute, Switzerland. The ARPES maps were recorded with a DA30 Scienta analyzer at an energy resolution of 30 meV and angular resolution of 0.1°. The samples were loaded *ex-situ* and measured in the ARPES setup without annealing. All measurements are acquired at 12 K in a base pressure of better than 5×10^{-11} Torr. Prior to the ARPES measurements, potassium was *in-situ* doped on the surface of insulating KTO wafers to induce the 2DEG and ground the surface. Proper photon energies were selected for all terminations to accurately probe the FS at the $k_z = 0$ plane, which is $hv = 80$ eV for (001) termiation, $hv = 60$ eV for (110) termination, and $hv = 108$ eV for (111) termination.

4.4 DFT:

5d perovskite oxide $KTaO_3$ dependent on layered orientations as several slab models was calculated based on the projector augmented wave method and the Perdew-Bruke-Ernzerhof revised for solids exchange potential implemented in Vienna ab initio simulation package. Spin-orbital coupling is self-consistent included in order to consider the relativistic effect. The energy cutoff was 520 eV with the $9 \times 9 \times 9$ and $11 \times 11 \times 1$ Gamma-center k grid for the Brillouin zone sample for bulk and slab models, respectively. (001), (110), and (111) crystalline directions slab structures are constructed with vertical vacuum layer length larger than 10 Å in order to reduce unreal interlayer effect. The selective dynamics method was used to fix partly atoms layer to be ideal subtracted factor with the other atoms layer fully relaxation. The irreducible representations of these relaxed slab models were calculated by irvsp code. Utilizing VASP2WANNIER interface, Wannier functions were got by projecting Ta-d and O-p orbitals to construct a simple tight-binding model. The corresponding band structures and surface weighted density of states were performed with WannierTools. The orbital projected band structures and spin-textures of slab structures with n=5 Ta layers based on a simple tight-binding method were calculated by combining the slab function of WannierTools to analysis the corresponding Wave function information and operator values.

Supporting Information is linked to the online version of the paper

Author contributions

Y.Z.C. designed the concept and experiments. H.X., Y.C.Z. and Y.L.G. fabricated the samples and performed magneto-transport characterization. H. L. performed the ARPES experiment and data analysis. X.J.C., L.S. and Z.C.Z.

performed the DFT calculations. N.G. D.J. and J.V. performed the STEM measurements and analysis. All authors discussed the results, interpretations, and wrote the manuscript.

References

[1] H. Y. Hwang, Y. Iwasa, M. Kawasaki, B. Keimer, N. Nagaosa, Y. Tokura, *Nat. Mater.* **2012**, *11*, 103.

[2] F. Trier, P. Noël, J.-V. Kim, J.-P. Attané, L. Vila, M. Bibes, *Nat. Rev. Mater.* **2021**, *7*, 258.

[3] Z. Huang, Ariando, X. Renshaw Wang, A. Rusydi, J. Chen, H. Yang, T. Venkatesan, *Adv. Mater.* **2018**, *30*, 1802439.

[4] A. D. Caviglia, M. Gabay, S. Gariglio, N. Reyren, C. Cancellieri, J.-M. Triscone, *Phys. Rev. Lett.* **2010**, *104*, 126803.

[5] Z. Zhong, A. Tóth, K. Held, *Phys. Rev. B* **2013**, *87*, 161102.

[6] G. Herranz, G. Singh, N. Bergeal, A. Jouan, J. Lesueur, J. Gázquez, M. Varela, M. Scigaj, N. Dix, F. Sánchez, J. Fontcuberta, *Nat. Commun.* **2015**, *6*, 6028.

[7] J. Varignon, L. Vila, A. Barthélémy, M. Bibes, *Nat. Phys.* **2018**, *14*, 322.

[8] E. Lesne, Y. Fu, S. Oyarzun, J. C. Rojas-Sánchez, D. C. Vaz, H. Naganuma, G. Sicoli, J.-P. Attané, M. Jamet, E. Jacquet, J.-M. George, A. Barthélémy, H. Jaffrès, A. Fert, M. Bibes, L. Vila, *Nat. Mater.* **2016**, *15*, 1261.

[9] L. M. Vicente‐Arche, J. Bréhin, S. Varotto, M. Cosset‐Cheneau, S. Mallik, R. Salazar, P. Noël, D. C. Vaz, F. Trier, S. Bhattacharya, A. Sander, P. Le Fèvre, F. Bertran, G. Saiz, G. Ménard, N. Bergeal, A. Barthélémy, H. Li, C. Lin, D. E. Nikonov, I. A. Young, J. E. Rault, L. Vila, J. Attané, M. Bibes, *Adv. Mater.* **2021**, *33*, 2102102.

[10] S. Manipatruni, D. E. Nikonov, C.-C. Lin, T. A. Gosavi, H. Liu, B. Prasad, Y.-L. Huang, E. Bonturim, R. Ramesh, I. A. Young, *Nature* **2019**, *565*, 35.

[11] M. Z. Hasan, C. L. Kane, *Rev. Mod. Phys.* **2010**, *82*, 3045.

[12] A. Ohtomo, H. Y. Hwang, *Nature* **2004**, *427*, 423.

[13] N. Reyren, S. Thiel, A. D. Caviglia, L. F. Kourkoutis, G. Hammerl, C. Richter, C. W. Schneider, T. Kopp, A.-S. Rüetschi, D. Jaccard, M. Gabay, D. A. Muller, J.-M. Triscone, J. Mannhart, *Science* **2007**, *317*, 1196.

[14] A. Brinkman, M. Huijben, M. Van Zalk, J. Huijben, U. Zeitler, J. C. Maan, W. G. Van Der Wiel, G. Rijnders, D. H. A. Blank, H. Hilgenkamp, *Nat. Mater.* **2007**, *6*, 493.

[15] G. Chen, L. Balents, *Phys. Rev. Lett.* **2013**, *110*, 206401.

[16] F. Trier, G. E. D. K. Prawiroatmodjo, Z. Zhong, D. V. Christensen, M. Von Soosten, A. Bhowmik, J. M. G. Lastra, Y. Chen, T. S. Jespersen, N. Pryds, *Phys. Rev. Lett.* **2016**, *117*, 096804.

[17] N. Nakagawa, H. Y. Hwang, D. A. Muller, *Nat. Mater.* **2006**, *5*, 204.

[18] Y. Chen, N. Pryds, J. E. Kleibeuker, G. Koster, J. Sun, E. Stamate, B. Shen, G. Rijnders, S. Linderoth, *Nano Lett.* **2011**, *11*, 3774.

[19] Y. Chen, R. J. Green, R. Sutarto, F. He, S. Linderoth, G. A. Sawatzky, N. Pryds, *Nano Lett.* **2017**, *17*, 7062.

[20] W. Meevasana, P. D. C. King, R. H. He, S.-K. Mo, M. Hashimoto, A. Tamai, P. Songsiriritthigul, F. Baumberger, Z.-X. Shen, *Nat. Mater.* **2011**, *10*, 114.

[21] P. D. C. King, R. H. He, T. Eknapakul, P. Buaphet, S.-K. Mo, Y. Kaneko, S. Harashima, Y. Hikita, M. S. Bahramy, C. Bell, Z. Hussain, Y. Tokura, Z.-X. Shen, H. Y. Hwang, F. Baumberger, W. Meevasana, *Phys. Rev. Lett.* **2012**, *108*, 117602.

[22] H. Liang, L. Cheng, L. Wei, Z. Luo, G. Yu, C. Zeng, Z. Zhang, *Phys. Rev. B* **2015**, *92*, 075309.

[23] P. K. Rout, E. Maniv, Y. Dagan, *Phys. Rev. Lett.* **2017**, *119*, 237002.

[24] W. Lin, L. Li, F. Doğan, C. Li, H. Rotella, X. Yu, B. Zhang, Y. Li, W. S. Lew, S. Wang, W. Prellier, S. J. Pennycook, J. Chen, Z. Zhong, A. Manchon, T. Wu, *Nat. Commun.* **2019**, *10*, 3052.

[25] G. J. Omar, W. L. Kong, H. Jani, M. S. Li, J. Zhou, Z. S. Lim, S. Prakash, S. W. Zeng, S. Hooda, T. Venkatesan, Y. P. Feng, S. J. Pennycook, L. Shen, A. Ariando, *Phys. Rev. Lett.* **2022**, *129*, 187203.

[26] K. Zou, S. Ismail-Beigi, K. Kisslinger, X. Shen, D. Su, F. J. Walker, C. H. Ahn, *APL Mater.* **2015**, *3*, 036104.

[27] F. Y. Bruno, S. McKeown Walker, S. Riccò, A. De La Torre, Z. Wang, A. Tamai, T. K. Kim, M. Hoesch, M. S. Bahramy, F. Baumberger, *Adv. Electron. Mater.* **2019**, *5*,

1800860.

[28] C. Liu, X. Yan, D. Jin, Y. Ma, H.-W. Hsiao, Y. Lin, T. M. Bretz-Sullivan, X. Zhou, J. Pearson, B. Fisher, J. S. Jiang, W. Han, J.-M. Zuo, J. Wen, D. D. Fong, J. Sun, H. Zhou, A. Bhattacharya, *Science* **2021**, *371*, 716.

[29] Z. Chen, Z. Liu, Y. Sun, X. Chen, Y. Liu, H. Zhang, H. Li, M. Zhang, S. Hong, T. Ren, C. Zhang, H. Tian, Y. Zhou, J. Sun, Y. Xie, *Phys. Rev. Lett.* **2021**, *126*, 026802.

[30] Z. Chen, Y. Liu, H. Zhang, Z. Liu, H. Tian, Y. Sun, M. Zhang, Y. Zhou, J. Sun, Y. Xie, *Science* **2021**, *372*, 721.

[31] Y. Gan, F. Yang, L. Kong, X. Chen, H. Xu, J. Zhao, G. Li, Y. Zhao, L. Yan, Z. Zhong, Y. Chen, H. Ding, *Adv. Mater.* **2023**, *35*, 2300582.

[32] H. Zhang, X. Yan, X. Zhang, S. Wang, C. Xiong, H. Zhang, S. Qi, J. Zhang, F. Han, N. Wu, B. Liu, Y. Chen, B. Shen, J. Sun, *ACS Nano* **2019**, *13*, 609.

[33] G. E. D. K. Prawiroatmodjo, F. Trier, D. V. Christensen, Y. Chen, N. Pryds, T. S. Jespersen, *Phys. Rev. B* **2016**, *93*, 184504.

[34] S. A. Chambers, M. H. Engelhard, V. Shutthanandan, Z. Zhu, T. C. Droubay, L. Qiao, P. V. Sushko, T. Feng, H. D. Lee, T. Gustafsson, E. Garfunkel, A. B. Shah, J.-M. Zuo, Q. M. Ramasse, *Surf. Sci. Rep.* **2010**, *65*, 317.

[35] C. Cantoni, J. Gazquez, F. Miletto Granozio, M. P. Oxley, M. Varela, A. R. Lupini, S. J. Pennycook, C. Aruta, U. S. Di Uccio, P. Perna, D. Maccariello, *Adv. Mater.* **2012**, *24*, 3952.

[36] D. E. E. Deacon‑Smith, D. O. Scanlon, C. R. A. Catlow, A. A. Sokol, S. M. Woodley, *Adv. Mater.* **2014**, *26*, 7252.

[37] M. Setvin, M. Reticcioli, F. Poelzleitner, J. Hulva, M. Schmid, L. A. Boatner, C. Franchini, U. Diebold, *Science* **2018**, *359*, 572.

[38] C. Liu, X. Zhou, D. Hong, B. Fisher, H. Zheng, J. Pearson, J. S. Jiang, D. Jin, M. R. Norman, A. Bhattacharya, *Nat. Commun.* **2023**, *14*, 951.

[39] E. A. Martínez, J. Dai, M. Tallarida, N. M. Nemes, F. Y. Bruno, *Adv. Electron. Mater.* **2023**, *9*, 2300267.

[40] S. McKeown Walker, A. De La Torre, F. Y. Bruno, A. Tamai, T. K. Kim, M. Hoesch, M. Shi, M. S. Bahramy, P. D. C. King, F. Baumberger, *Phys. Rev. Lett.* **2014**, *113*, 177601.

[41] S. Varotto, A. Johansson, B. Göbel, L. M. Vicente-Arche, S. Mallik, J. Bréhin, R. Salazar, F. Bertran, P. L. Fèvre, N. Bergeal, J. Rault, I. Mertig, M. Bibes, *Nat. Commun.* **2022**, *13*, 6165.

[42] A. F. Santander-Syro, C. Bareille, F. Fortuna, O. Copie, M. Gabay, F. Bertran, A. Taleb-Ibrahimi, P. Le Fèvre, G. Herranz, N. Reyren, M. Bibes, A. Barthélémy, P. Lecoeur, J. Guevara, M. J. Rozenberg, *Phys. Rev. B* **2012**, *86*, 121107.

[43] J.-H. Park, C. H. Kim, J.-W. Rhim, J. H. Han, *Phys. Rev. B* **2012**, *85*, 195401.

[44] S. R. Park, C. H. Kim, J. Yu, J. H. Han, C. Kim, *Phys. Rev. Lett.* **2011**, *107*, 156803.

[45] M. R. Scholz, J. Sánchez-Barriga, J. Braun, D. Marchenko, A. Varykhalov, M. Lindroos, Y. J. Wang, H. Lin, A. Bansil, J. Minár, H. Ebert, A. Volykhov, L. V. Yashina, O. Rader, *Phys. Rev. Lett.* **2013**, *110*, 216801.

[46] C. Cancellieri, A. S. Mishchenko, U. Aschauer, A. Filippetti, C. Faber, O. S. Barišić, V. A. Rogalev, T. Schmitt, N. Nagaosa, V. N. Strocov, *Nat. Commun.* **2016**, *7*, 10386.

[47] Y. Z. Chen, F. Trier, T. Wijnands, R. J. Green, N. Gauquelin, R. Egoavil, D. V. Christensen, G. Koster, M. Huijben, N. Bovet, S. Macke, F. He, R. Sutarto, N. H. Andersen, J. A. Sulpizio, M. Honig, G. E. D. K. Prawiroatmodjo, T. S. Jespersen, S. Linderoth, S. Ilani, J. Verbeeck, G. Van Tendeloo, G. Rijnders, G. A. Sawatzky, N. Pryds, *Nat. Mater.* **2015**, *14*, 801.

[48] H. Li, Y. Gan, M.-A. Husanu, R. T. Dahm, D. V. Christensen, M. Radovic, J. Sun, M. Shi, B. Shen, N. Pryds, Y. Chen, *ACS Nano* **2022**, *16*, 6437.

[49] X. Chen, T. Yu, Y. Liu, Y. Sun, M. Lei, N. Guo, Y. Fan, M. Zhang, F. Alarab, V. N. Strokov, Y. Wang, T. Zhou, X. Liu, F. Lu, W. Liu, Y. Xie, R. Peng, H. Xu, D. Feng, arXiv:2301.13488

[50] G. Khalsa, B. Lee, A. H. MacDonald, *Phys. Rev. B* **2013**, *88*, 041302.

[51] L. Yuan, Q. Liu, X. Zhang, J. W. Luo, S. S Li, A. Zunger, Nature Commun. **2019**, 10, 906.

[52] D. Xiao, W. Zhu, Y. Ran, N. Nagaosa, S. Okamoto, *Nat. Commun.* **2011**, *2*, 596.

[53] J. Verbeeck, S. Van Aert, *Ultramicroscopy* **2004**, *101*, 207.

[54] W. Van Den Broek, D. Jannis, J. Verbeeck, *Ultramicroscopy* **2023**, *254*, 113830.

[55] J. Verbeeck, S. Van Aert, G. Bertoni, *Ultramicroscopy* **2006**, *106*, 976.

[56] Z. Z. Zhang, I. Lobato, D. Jannis, J. Verbeeck, S. V. Aert, P. Nellist. *Zenodo* **2023**.